ELSEVIER

Biochimica et Biophysica Acta 1230 (1995) 51–61

BBA Biochimica et Biophysica Acta

Optically detected magnetic field effects on reaction centers of *Rhodobacter sphaeroides* 2.4.1 and its Tyr M210 → Trp mutant

Robert van der Vos [a], Eric M. Franken [a], Stephen J. Sexton [b], Susana Shochat [a], Peter Gast [a], P.J. Hore [b], Arnold J. Hoff [a,*]

[a] *Department of Biophysics, Huygens Laboratory, Leiden University, P.O. Box 9504, 2300 RA Leiden, The Netherlands*
[b] *Physical Chemistry Laboratory, Oxford University, South Parks Road, Oxford, OX1 3QZ, UK*

Received 18 August 1994; revised 8 February 1995; accepted 8 March 1995

Abstract

In this work, the magnetic field effects (MFE) on the triplet yield in reaction centers (RCs) of *Rhodobacter* (*Rb.*) *sphaeroides* 2.4.1 and its Tyr M210 → Trp mutant are compared. The MFE is measured between 25 and 225 K by monitoring the absorbance. Using monochromatic polarised and unpolarised light, linear dichroic (LD-)MFE curves were obtained. Simulations of the (LD-) MFE measured at low temperatures (25 K) are presented, which suggest that the exchange interaction in the mutant and in the wild type have opposite sign. This is explained by considering the free energy differences between the excited primary donor state $^1P^*$ and the charge-separated state. The magnetic field dependence of the MFE of Q-depleted mutant RCs at low magnetic fields is similar for temperatures between 25 and 225 K, implying that k_T is practically temperature independent. This suggests that the temperature dependence of the triplet yield is due to a change in radical pair singlet recombination rate k_S. The exchange interaction between the oxidised primary donor and reduced intermediary bacteriopheophytin acceptor of mutant RCs is twice as large as that of the wild type. This is attributed to an upward change of the energy level of the charge-separated state caused by the mutation.

Keywords: Exchange interaction; Mutant; Magnetic field effect; Photosynthesis; Reaction center

1. Introduction

A few years ago, we developed magneto-optical difference spectroscopy (MODS), in which the excited triplet and singlet ground state populations of the complex under study were varied by applying a magnetic field modulated sinusoidally with frequency f [1]. The population modulation was detected by monitoring the transmittance, which is modulated by the magnetic field when the ground state absorbance is different from the triplet absorbance. Using MODS, highly accurate triplet-minus-singlet (T − S) spectra can be measured from cryogenic temperatures to room temperature in a relatively simple way. However, the triplet concentration as a function of the applied magnetic field (B) is not measured properly with this technique, since the 2f Fourier component of the change in transmittance is detected, which corresponds to the actual magnetic field effect (MFE) only for small modulation amplitudes.

We show below that utilizing a field-sweep technique combined with small-amplitude field modulation (as is commonly used in for example Electron Paramagnetic Resonance spectroscopy), accurate curves of the MFE vs. B (MFE-curves) are obtained with high resolution. We have applied this method to study MFE-curves of a mutant of *Rhodobacter* (*Rb.*) *sphaeroides* as a function of temperature. Tyrosine M210 in the reaction center (RC) of *Rb. sphaeroides* is in van der Waals-contact with the primary donor P, and is close to the accessory bacteriochlorophyll B_A and the primary acceptor ϕ_A [2]. It has therefore been implicated as an important factor in primary electron transport [Refs. in 3]. Replacing Tyr M210 by a

Abbreviations: B_A, accessory bacteriochlorophyll in the active chain; LD, lineair dichroic; MFE, magnetic field effect; MIMS, magnetic-field induced mixing of triplet sublevels; MODS, magneto-optical difference spectroscopy; P, primary electron donor; PC, personal computer; PEM, photoelastic modulator; Q, quinone; Q_A, first acceptor quinone; RC, reaction center; RP, radical pair; , RPM, radical pair mechanism; T − S, triplet-minus-singlet; Φ_A, baceriopheophytin in the active chain.

* Corresponding author. Fax: +31 71 275819.

SSDI 0005-2728(95)00039-9

number of non-aromatic and/or non-polar residues indeed produced considerable changes in the electron transport properties [4–6]. These studies prompted us to study the electron transport properties of a Tyr M210 mutant for which the aromaticity was *increased*. Recently, we have constructed the M210 Tyr → Trp mutant, and studied electron transfer with fast laser spectroscopy [3]. It was found that at room temperature charge separation was biphasic with rates of $(36\ \text{ps})^{-1}$ (75%) and $(3\ \text{ps})^{-1}$ [3], whereas at cryogenic temperatures charge separation was mono-exponential with rate $(300\ \text{ps})^{-1}$ [7]. The MFE-curve measured with the direct-detection technique described in [8] showed a clear so-called $2J$-resonance for temperatures of 100 K and lower [9]. In contrast, for RCs of *Rb. sphaeroides* wild type (by which we mean the *Rb. sphaeroides* 2.4.1 deletion strain complemented with the plasmid bearing the wild type genes, from which the mutant was prepared), no clear $2J$-resonance was observed between 150 and 240 K [10], consistent with the much smaller value of $2J = 1.4$ mT obtained with RYDMR spectroscopy for Q-depleted RCs of *Rb. sphaeroides* R-26 over this temperature range (reviewed in [11]). In view of the slow charge-separation kinetics of the Tyr M210 → Trp mutant, its large exchange interaction is quite surprising.

In this work we compare MFE-curves, measured with the field-sweep technique, of RCs of the M210 Tyr → Trp mutant, of *Rb. sphaeroides* wild type, and of mutant RCs from which the acceptor quinones were removed (Q-depleted RCs), at low and high temperatures. In addition, we present for all three RCs linear-dichroic (LD) MFE-curves, representing the difference between the MFE-curves measured with the polarisation direction of excitation/probe light parallel and perpendicular to B. The MFE- and LD-MFE-curves at low temperatures are simulated using a model including the Magnetic field-Induced Mixing of the Sublevel wavefunctions of the primary donor triplet ^{3}P (MIMS, [8]), and the change in ^{3}P-yield due to the influence of the magnetic field on the efficiency of singlet-triplet (S-T) mixing (the radical pair mechanism), which effect we label the RPM-MFE.

2. Theory

Excitation of P leads to charge separation by fast electron transfer ($0.3\ \text{ps}^{-1}$) from P to the primary acceptor (Φ_A) [12], creating the primary radical pair ($P^+\Phi_A^-$). In vivo, the electron of Φ_A^- is transferred to a secondary acceptor, a quinone (Q_A), from which further electron transport is relatively slow ($\sim 100\ \mu$s). When electron transfer to the secondary acceptor is inhibited, for example by removing or pre-reducing the quinone, the electron remains located on the primary acceptor Φ_A and the radical pair lifetime is no longer determined by the $P^+\Phi_A^-Q_A \rightarrow P^+\Phi_A Q_A^-$ transfer rate, but by the recombination rates to the primary donor triplet (^{3}P) and singlet ground

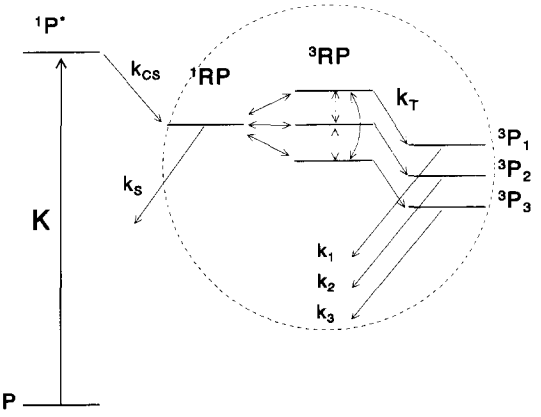

Fig. 1. Schematic drawing of the energy levels involved in the charge separation and triplet formation. The double-headed arrows (↔) linking the levels of the ^{1}RP and ^{3}RP levels represent the hyperfine interaction.

state (P), k_T and k_S, respectively. The recombination from ^{3}RP to ^{3}P is assumed to occur with conservation of spin angular momentum and with equal rates (k_T) for the three eigenstates of ^{3}P:

$$^3RP_i \xrightarrow{k_T} {}^3P_i,\ i = 1,2,3 \qquad (1)$$

where i labels the eigenstates of ^{3}P, and ^3RP_i represents the projection of the radical pair density matrix onto the i-th eigenfunction of ^{3}P. Clearly, this projection depends on the relative orientation of the triplet axes system of ^{3}P and ^{3}RP. We have found that for values of the ^{3}RP dipolar interaction $D_{P\Phi}$ lower than say 0.5 mT, the simulations were not sensitive to the actual value of $D_{P\Phi}$, which was therefore set to zero for most of our calculations. This procedure speeded up the simulations considerably, as then the relative orientation of ^{3}P and ^{3}RP is irrelevant.

In Fig. 1, we have drawn the energy scheme for the case where electron transfer to the secondary electron acceptor is blocked. The double-headed arrows between the radical pair singlet (^{1}RP) and triplet (^3RP_i, $i = 1,2,3$) states represent non-zero transition probabilities. The radical pair is generated from $^1P^*$ in the singlet electron spin state. Its evolution in time is determined by the radical pair Hamiltonian, and k_S and k_T, which together govern the time dependence of the electron spin density matrix ρ, describing the ensemble of radical pairs [13–15]. As the frequency of the modulation is slow compared to the dynamics of the system, the observed modulation of the transmittance results from changes in steady-state concentrations. The kinetic scheme, depicted in Fig. 1, can be expressed mathematically in a set of differential equations, including the stochastic Liouville equation for ρ. Under steady-state conditions, all time-derivatives are zero, and the set of equations can be solved. The rate of formation of ^{3}P in state i is $k_T[^3RP_i]$, and its rate of disappearance is $k_i[^3P_i]$, where k_i is the decay rate of state i (see Fig. 1) and the square brackets indicate steady-state concentra-

tions. The total ^3P concentration (the observable in our experiments) is thus

$$[^3P] = \sum_{i=1}^{3} [^3P_i] = k_T \sum_{i=1}^{3} \frac{[^3RP_i]}{k_i}, \quad i = 1,2,3 \tag{2}$$

To calculate $[^3RP_i]$ and k_i, it is convenient to use as basis states the zero-field spin eigenfunctions of ^3P. These wavefunctions ($|T_x\rangle$, $|T_y\rangle$, and $|T_z\rangle$) are related to the eigenstates of ^3P in non-zero field by

$$|T_i\rangle = \sum_{\alpha=x,y,z} a_{i\alpha}(B)|T_\alpha\rangle \tag{3}$$

where the coefficients $a_{i\alpha}(B)$ are obtained by diagonalization of the triplet Hamiltonian, and depend on the magnetic field B as well as on the zero-field splitting parameters D and E. Using this transformation, we have

$$k_i = \sum_{\alpha=x,y,z} a_{i\alpha}(B)a^*_{i\alpha}(B)k_\alpha, \tag{4}$$

where the triplet rates k_x, k_y, and k_z are known [16], and

$$[^3RP_i] = I_{abs} \sum_{\alpha=x,y,z} \sum_{\beta=x,y,z} a_{i\beta}(B)a^*_{i\alpha}(B)\rho_{\alpha\beta} \tag{5}$$

where $\rho_{\alpha\beta}$ is a matrix element of the radical pair density matrix operator, evaluated in the eigenbasis of the zero-field Hamiltonian of ^3P: $\rho_{\alpha\beta} = \langle T_\alpha|\rho|T_\beta\rangle$, $\alpha,\beta = x,y,z$. I_{abs} is the steady-state rate of production of singlet radical pairs (see later). The density operator ρ is obtained from the stochastic Liouville equation, including the Zeeman, hyperfine, exchange and dipolar interactions in the radical pair, the kinetics of the $^1RP \rightarrow P$ and $^3RP_i \rightarrow {}^3P_i$ steps, and the formation of the radical pair in its singlet state. When calculating MFE-curves for Q-reduced RCs, we have refrained from including in the formalism the presence of unpaired electrons on Q_A^- and on Fe^{2+} as this would have made the simulations prohibitively time consuming.

Qualitatively, the effect of the magnetic field can be described as follows: The Zeeman effect causes the ^3RP levels with magnetic spin quantum numbers $m = +1$ and -1 to separate from the ^1RP state. In other words, the field changes the Hamiltonian of the radical pair, by which the elements of the spin density matrix, and thus the radical pair triplet populating probabilities, change. In general, the populating probability of the ^3RP levels with $m = \pm 1$ levels will decrease because the difference between their energy and that of the ^1RP level becomes larger. Furthermore, as the zero-field decay rates k_α ($\alpha = x,y,z$) are not equal, applying a magnetic field will change the decay rates of the triplet levels, and thus the steady-state concentration of triplet level ^3P_i.

So far, we have neglected the anisotropy of ^3P and ^3RP. This anisotropy is due to the dipolar interaction, through which the MFE becomes dependent on the orientation of the triplet-carrying RC relative to the magnetic field axis [17]. The triplet concentration given by Eq. 2 is therefore specific for an RC with a particular orientation relative to the laboratory frame, defined by the polar angles θ and ϕ.

A second anisotropy is introduced by applying polarized light for excitation and detection. (In the experimental set-up, a single excitation/probe beam is used, see next section.) The excitation rate I_{abs} then depends on the angle between the polarisation direction of the exciting light $\vec{\nu}$ and the optical transition moment $\vec{\mu}$:

$$I_{abs} \propto |\vec{\mu} \cdot \vec{\nu}|^2. \tag{6}$$

Finally, the observed absorbance dA/dB may be calculated from

$$A = \langle [P]|\vec{\mu} \cdot \vec{\nu}|^2 \rangle \tag{7}$$

where $\langle \ldots \rangle$ indicates an orientational average. [P] is the steady-state concentration of ground state primary donor, obtained from $[P] + [^3P] = \text{constant}$ (because $[^1P^*], [RP] \ll [P], [^3P]$).

The simulated curves of Figs 7 and 8 (see discussion), have been calculated using the above formalism. It is difficult, however, to appreciate the origin of the salient features of the MFE- and LD − MFE-curves from the numerical calculations. In the Appendix, we therefore present a simplified analytical treatment, which reproduces the main features of the low-temperature MFE-curves.

3. Experimental

The M210 Tyr → Trp mutant was constructed, and RCs of the mutant and of *Rb. sphaeroides* isolated, as in Ref. 3. Samples were diluted to 66% glycerol to ensure the formation of a clear glass. The final optical absorbance of the sample measured at 800 nm at room temperature varied between 0.4 and 0.7. In Q-containing RCs the (primary) quinone was reduced by adding 10 mM ascorbate and freezing under illumination.

The field-modulation experiments were carried out with a home-built water-cooled magnet with two pairs of coils for the AC- and DC-magnetic field. For the AC coils we used 100 turns and for the DC-coils 500 turns of copper wire with a diameter of 1 mm (for dimensions, see Fig. 2). The magnetic field, calibrated with a Hall-meter, was found to be 10.0 mT/A for the DC-coils and 1.0 mT/A for the AC-coils. The modulation amplitude of the AC magnetic field was 0.2-0.5 mT, depending on the step size used in incrementing the DC magnetic field. With the DC-coils a maximum magnetic field of approx. 60 mT could be obtained. The current of the alternating magnetic field was supplied by a home-built sweep current amplifier (35 Hz-1 kHz), fed by a Tektronix CFG 250 function generator. The DC-current up to 4 A was supplied by an Oltronix power supply B32-10R programmed by the voltage from a digital-to-analogue converter, which was set by the measurement program running on a personal computer (PC).

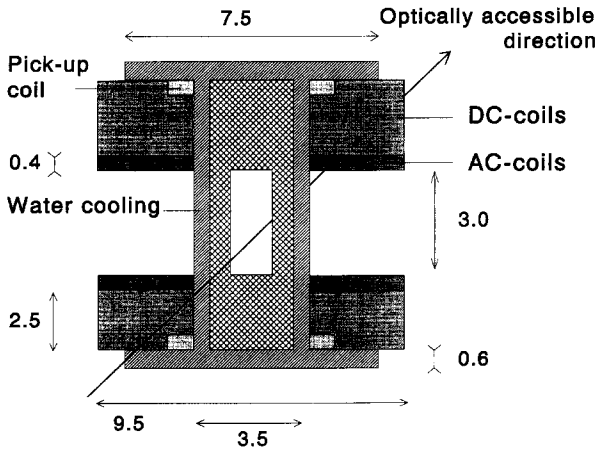

Fig. 2. The water-cooled magnet with separate AC and DC coil pairs. The coils were wound with 1 mm diameter copper wire. For the AC coils 100, and for the DC coils 500 turns were used. Dimensions in cm.

The optical and cryogenic parts of the set-up were essentially the same as in Lous and Hoff [8,17,18]. The MFE-curves were measured by monitoring the absorbance band of the primary donor, using an AL896 interference filter in the actinic light beam to minimize heating of the sample (incident light intensity 250 mW/cm^2). The temperature was measured in the light spot with a BAV 99 diode biased with a 10 μA current as decribed in [19,20]. The temperatures given are accurate to ± 5 K. White light intensities were kept below 0.2 W/cm^2 when measuring (LD-) T − S spectra at low temperatures.

The anisotropy in the MFE was measured by inserting a photoelastic modulator (PEM) and an analyzer between the sample and the monochromator, and using an additional lock-in amplifier to demodulate the 100 kHz modulation of the PEM. Alternatively, a polarizer was inserted between the lamp and the sample, and the MFE measured with the polarizer oriented parallel and perpendicular to the magnetic field. Although the excitation of the sample is then no longer isotropic, this method has the important advantage that the determination of $MFE_{\parallel} - MFE_{\perp}$ is now direct, and baseline errors are largely cancelled, because they are approximately the same for the MFE measured with light polarised parallel and perpendicular to the magnetic field.

Electronic detection was performed by a EG and G 5209 lock-in amplifier, which was interfaced by an IEEE bus to the PC. The LD-(T − S) signals were detected using an EG and G 5209 (100 kHz) and an EG and G 5101 (frequency of the magnetic field modulation) lock-in amplifier in series. The output of the latter was connected to an analogue-to-digital-converter that was read by the PC.

The MFE simulations were carried out on a SUN Sparc-2 workstation. The density operator of the radical pair was calculated using a two-proton approximation, with the hyperfine interactions having a Gaussian distribution for the three canonical directions. The stochastic Liouville equation was solved using a standard routine from the Numerical Algorithms Group (NAG) library. For the simulations of the low-temperature MFE-curves, the triplet yield as a function of the magnetic field was evaluated for 480 different reaction center orientations. Simulations were performed using an anisotropic radical pair triplet (the zero-field splitting parameter D of the radical pair, $D_{PI} \approx 0.5$ mT), and with an isotropic radical pair ($D_{PI} = 0$). The latter approximation greatly accelerated the calculations, and resulted in only minor differences with the result when D_{PI} was included. The values of the kinetic parameters used for the simulations are listed in the captions of Figs. 7 and 8.

4. Results

The derivatives of the MFE-curves recorded at 25 K for RCs of *Rb. sphaeroides* wild type, the mutant and Q-depleted RCs of the mutant are shown in Fig. 3. Henceforth, unless otherwise specified, the labels MFE and LD-MFE will designate the *derivative* of the respective curves. The LD-MFE was recorded using a PEM between the sample and the monochromator, and unpolarised excitation. For

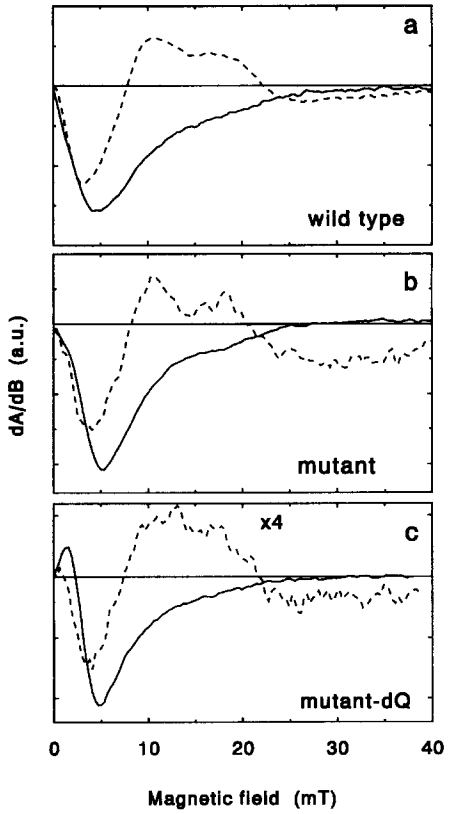

Fig. 3. Derivative isotropic MFE (solid line) and LD-MFE (dashed line) recorded at 25 K, using a PEM with analyser between the sample and the light detector. The (LD-) MFE-curves are shown for (a) RCs the wild type of *Rb. sphaeroides*. (b) RCs of the Tyr M210 → Trp mutant. (c) Q-depleted RCs of the Tyr M210 → Trp mutant.

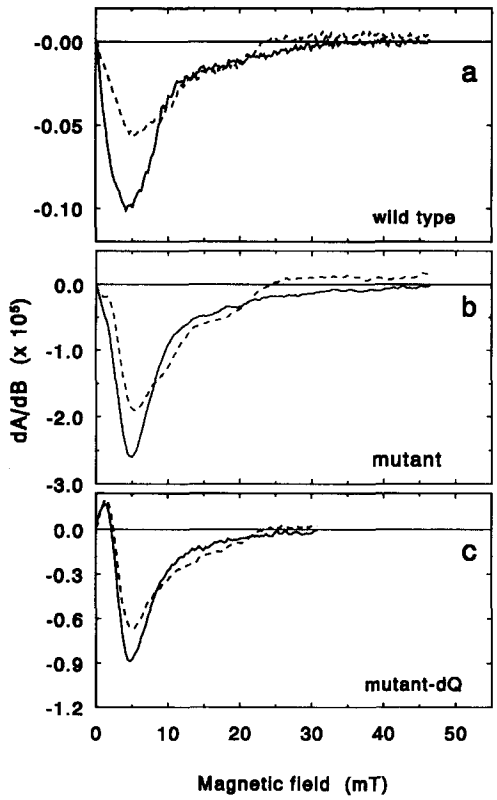

Fig. 4. Derivative $MFE_{\|}$ (drawn line) and $MFE_{\perp}$ (dashed line) recorded at 25 K, with a polariser between the lamp and the sample. The MFE-curves are shown for (a) RCs the wild type of *Rb. sphaeroides*. (b) RCs of the Tyr M210 → Trp mutant. (c) Q-depleted RCs of the Tyr M210 → Trp mutant.

obtaining more insight in the origin of the structure of the LD-MFE curves, the low-temperature MFE-curve for RCs of the wild type and the mutant with and without quinone were recorded using excitation light polarised parallel and perpendicular to the magnetic field ($MFE_{\|}$ and $MFE_{\perp}$, respectively). The resulting curves are displayed in Fig. 4. Because in these experiments the intensity of the light incident on the sample was halved, the curves are somewhat noisier than those recorded with unpolarized light, and the difference between $MFE_{\|}$ and $MFE_{\perp}$ is less reliable than the LD-MFE curve in Fig. 3.

The MFE-curves of Q-reduced RCs show more structure than those of the Q-depleted RCs. This additional structure is also observed in the LD-MFE-curve where it appears as a double maximum in the positive part (Fig. 3a and b). For Q-depleted RCs, the double maximum in the LD-MFE is less pronounced compared to Q-reduced RCs, and the amplitude of the positive LD-MFE relative to the minimum is larger than for Q-reduced RCs. Fig. 4 shows that the additional structure is mainly due to the $MFE_{\perp}$. Minima or shoulders at 5.3, 9.3 and 19.6 mT can be discerned. For all RCs, the $MFE_{\perp}$-curve crosses the baseline at approx. 25 mT and from there on shows an increasing triplet concentration. The $MFE_{\|}$-curve does not show this effect. An important difference between the low-temperature MFE-curve for Q-reduced and Q-depleted RCs is the presence of a $2J$-resonance for Q-depleted RCs. For Q-reduced RCs, this maximum is only observable as a shoulder. The $2J$-resonance is barely observable in the LD-MFE-curve of Q-depleted RCs (Fig. 3c).

Apart from the $2J$-resonance, the positions where the (LD-)MFE changes sign or reaches an extreme value show very little variation for the wild type and the mutant with or without quinone. For all RCs, the two zero-crossings of the LD-MFE are located at 8.3 and 20.8 mT. Only a small variation of the location of the first minimum of the MFE- and LD-MFE-curves is observed; for RCs of the wild type this minimum is at 4.2 and 3.3 mT, for the mutant at 5 and 4.2 mT, respectively . Fig. 5 shows the MFE-curves recorded at 125 K for Q-reduced RCs of the wild type and for Q-reduced and Q-depleted RCs of the mutant. At this temperature, the MIMS-effect is negligible, because of the fast thermal equilibration of the triplet sublevels. As the lifetime of the radical pair is short on the time-scale of the equilibration processes, even for higher temperatures, the RPM-MFE is still observable. For both RCs, the MFE-curve is now quite smooth compared to that recorded at 25 K. Furthermore, the LD-MFE has become very small. The $MFE_{\|}$- and $MFE_{\perp}$-curves for both the mutant and the wild type (not shown) are as structureless as the MFE-curves of Fig. 5. Note that the MFE-curve for Q-reduced RCs of the wild type is identical to that of Q-reduced RCs of *Rb. sphaeroides* R-26 [17], which in turn is identical to that of Q-depleted RCs of *Rb. sphaeroides* R-26 [10], all measured at similar temperatures. Furthermore, the MFE-curves of Q-reduced RCs of the wild type and the mutant at 125 K are very different (Fig. 5), whereas the MFE-curves for the Q-reduced and Q-depleted RCs of the mutant are, apart from a scaling factor due to a difference in triplet yield,

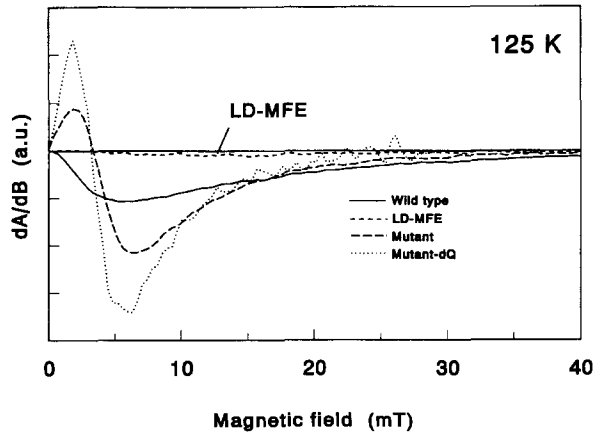

Fig. 5. Derivative MFE recorded at 125 K using isotropic excitation/probe light and a PEM between the sample and light detector for RCs of the wild type of *Rb. sphaeroides* (drawn line) RCs of the Tyr M210 → Trp mutant (long-dashed line) and Q-depleted RCs of the Tyr M210 → Trp mutant (dotted line). The short-dashed line indicates the derivative LD-MFE of RCs of *Rb. sphaeroides* wild type, also recorded at 125 K.

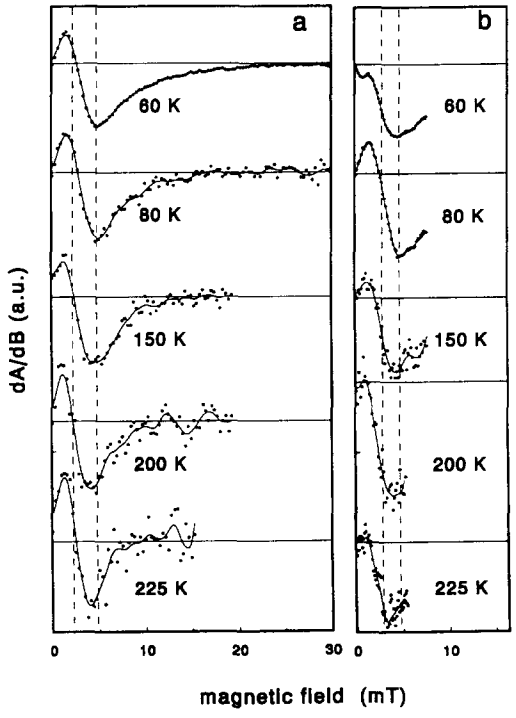

Fig. 6. Derivative MFE between 60 and 225 K for Q-depleted (a) and Q-reduced (b) RCs of the Tyr M210 → Trp mutant. Drawn curves: smoothed 5-point average. Dashed verticals are a guide to the eye.

identical. These observations demonstrate that the remarkable 2 J-resonance observed for the mutant as compared to its virtual absence in the MFE-curve for Q-reduced RCs of the wild type (Fig. 5), is not related to the presence or absence of the quinone, but to a property intrinsic to the TyrM210Trp mutation. The temperature dependence of the MFE-curves is shown in Fig. 6. The vertical amplitudes are normalized, as these depend on the triplet yield and on the efficiency of triplet–triplet transfer to the RC carotenoid, both of which are strongly temperature dependent (see e.g. [21,22]). For the MFE-curve of Q-depleted RCs of the mutant Fig. 6a shows that over the whole temperature range, the magnetic field strength at which the MFE crosses zero or reaches a minimum (4.7 mT) shows little variation with temperature. The field strength at which the (derivative) MFE-curve first crosses the baseline (the 2 J-resonance) is 2.3 mT below 60 K, 2.7 mT between 60 K and 100 K, decreases slightly at approx. 0.1 mT per 25 K, to 2.3 mT at 200 K, then increases to 2.6 mT at 225 K. The only parameter that changes considerably with temperature is the magnetic field strength at which the MFE saturates (defined as the magnetic field at which the MFE curve, obtained by numerical integration from the observed derivative MFE-curve, attains 90% of its high-field ($B > 50$ mT) amplitude). This is 25 mT at 25 and 40 K, approx. 22 mT at 80 K, and decreases to about 12 ± 2 mT at 225 K. The relative amplitude of the negative extremum of the MFE-curve relative to the 2 J-resonance becomes smaller with increasing temperature: at 80 K the ratio is 2 : 1, at 225 K it is 1 : 1.

The influence of the presence of a (negatively charged) quinone on the temperature dependence of the MFE is dramatic, as demonstrated in Fig. 6b, which shows a temperature study of the MFE-curve for Q-reduced RCs of the mutant. It is seen that going from high to low temperatures, the MFE-curve 'smoothes out'; the amplitude of the low-field maximum changes, and the baseline crossing connected with the 2 J-resonance shifts to higher field strengths.

5. Discussion

5.1. Simulation of the low-temperature LD-MFE-curve

Fig. 7 shows the simulated MFE-curves at low temperatures for RCs of *Rb. sphaeroides* wild type. The curves of Fig. 7 mimic quite well the characteristics of the experimental MFE-curves: for the LD-MFE curve, the large negative peak at 3 mT, a broader, positive maximum at 12 mT, two zero-crossings at 9 and 20 mT and a 'tail' that slowly decreases to zero on going to higher field values are all well simulated. The position of the second zero-crossing is closely related to the value of the zero-field splitting parameter |D| of the primary donor triplet (about 20.0 mT, see Appendix).

The $MFE_{\parallel}$ and $MFE_{\perp}$ curves in Fig. 7, simulated for $J = +0.7$ mT, fall off rapidly with increasing value of B for $B < 1$ mT. When taking $J = -0.7$ mT, and keeping the other parameters the same, the curves show a pronounced convexity (negative curvature) in this range of B,

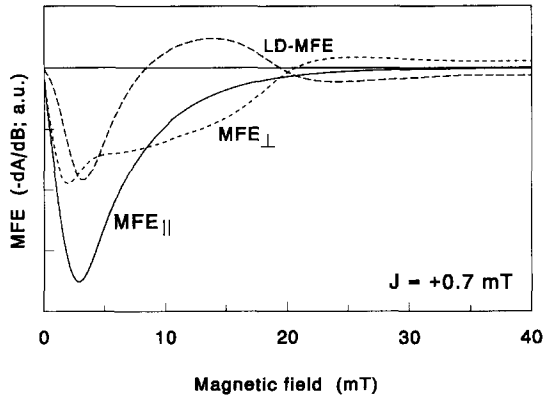

Fig. 7. Simulation of the low-temperature derivative (LD-)MFE for RCs of *Rb. sphaeroides* wild type. Drawn line: $MFE_{\parallel}$; short-dashed line: $MFE_{\perp}$; long-dashed line: LD-MFE. Parameters of the radical pair $J = +0.7$ mT, $k_S = 8 \cdot 10^6$ s^{-1}, $k_T = 6 \cdot 10^8$ s^{-1}, $D_{PI} = 0$ G. Hyperfine interactions: full widths of the Gaussian distributions of hyperfine couplings in each of the three directions x,y,z P^+, 0.57 mT; I^-, 0.75 mT, giving effective hyperfine couplings of 0.99 and 1.30 mT for P^+ and I^-, respectively. Parameters of the primary donor triplet [3]: $|D| = 20$ mT, $|E| = 3.5$ mT, $k_x = k_y = 8000$ s^{-1}, $k_z = 1200$ s^{-1}, the optical Q_y transition moment is taken to be oriented parallel to the triplet y-axis.

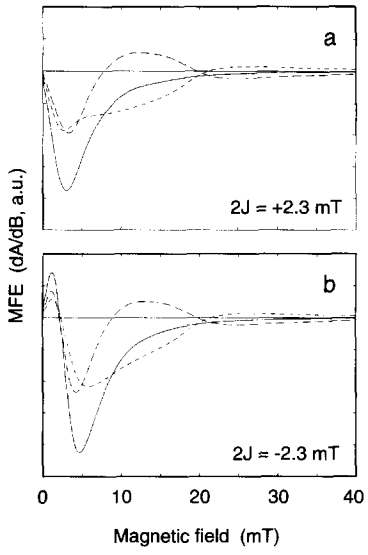

Fig. 8. Simulation of the low-temperature derivative (LD-)MFE for RCs of the mutant with a $2J$-value of (a) +2.3 mT and (b) −2.3 mT. $k_S = 3 \cdot 10^6$ s^{-1}, all other parameters and curve labels are equal to those of Fig. 7.

i.e. they fall off much less rapidly with B (not shown), and do not fit the experimental data at all. The sign of J for *Rb. sphaeroides* wild type inferred from this difference in the shape of the MFE-curves ($J > 0$), agrees with the sign of J determined for RCs of *R. rubrum* from Electron Spin Polarization experiments [23].

Apart from the pronounced $2J$-resonance, the low-temperature LD-MFE-curve of Q-depleted RCs of the mutant is similar to that of the wild type. This is not surprising, as with ADMR the primary donor triplet of the mutant was found to have zero-field splitting parameters, triplet sublevel kinetics and a triplet polarisation pattern very similar to those of the wild type [3]. The $2J$-resonance can be simulated quite well. Fig. 8 shows the simulation of the (LD)-MFE-curves of Q-depleted mutant RCs for a positive and a negative J-value (J is defined such that $E_S - E_T = +2J$, with E_S and E_T the energies of the radical pair singlet and triplet levels, respectively). The 'best-fit' values for the low-temperature radical pair recombination rates k_S and k_T are similar to those found for wild type RCs (Fig. 7). This tallies with the observation that the lifetime of the RP in the mutant at room temperature, about 30 ns (unpublished results), is similar to that for the wild type (about 10 ns, [24]). It is seen from Fig. 8 that the MFE-curves only show a $2J$-resonance when J is negative, resulting in the ^{3}RP state having a higher energy than the ^{1}RP state. The source of this effect can be traced to Eq. 5, which shows how the radical pair populations projected onto the eigenstates of ^{3}P are related to the elements of the radical pair density operator in the zero-field basis. Although the diagonal elements of ρ, which correspond to populations of states, do not depend on the sign of J (taking $D_{PI} = 0$), the off-diagonal elements (coherences between states) do. This is essentially the same reason why the phase of the electron spin polarization generated in a radical pair depends on the sign of its exchange interaction. To be a little more precise:

$$\text{when } J \rightarrow -J, \text{ then } \rho_{\alpha\alpha} \rightarrow \rho_{\alpha\alpha} \text{ and } \rho_{\alpha\beta} \rightarrow \rho^*_{\alpha\beta} = \rho_{\beta\alpha} \tag{8}$$

This change in the off-diagonal density matrix elements evidently modifies [^{3}RP$_i$] (see Eq. 5) and hence the simulated MFE-curve.

The negative sign of J is quite surprising, as the exchange interaction in RCs of *R. rubrum* [23] and of *Rb. sphaeroides* wild type (see above) is positive. It seems that, in addition to having a larger value, the exchange interaction has changed sign. Below, we will discuss the change in exchange interaction in relation to the free energy change of the $P^+B_A^-\Phi_A$ and $P^+B_A\Phi_A^-$ states, induced by the mutation.

5.2. The high-temperature MFE-curve

The MFE-curves of the mutant RCs measured at temperatures above 60 K (Fig. 6a) show three notable features: (i) A $2J$-resonance, located at 2.3 mT at 60 K, which shifts only slightly on going to higher temperatures. The amplitude of the maximum in the derivative MFE-curve that is connected to the $2J$-resonance, relative to the minimum of the curve is more or less conserved throughout the temperature range of 60 to 225 K. (ii) The minimum of the derivative MFE-curve, corresponding to the inflection point of the MFE-curve, remains approx. at the same position, 5.0 mT. (iii) The magnetic field at which the MFE is for more than 90% saturated as determined from the integrated derivative-MFE, becomes smaller with increasing temperature.

The practically temperature-independent value of B at the inflection point of the MFE-curve, B_{inf}, contrasts with observation (*iii*). The constant values of B_{inf} and $2J$, and of the relative amplitudes of the positive extremum at $B = J$ and the minimum at $B = B_{inf}$, show that the shape of the MFE-curve for $B \leq B_{inf}$ does not change much with temperature; only its amplitude becomes smaller. This is in agreement with the simulations performed by Werner and Schulten ([12], also shown in [14]), who simulated the RPM-MFE curves. The simulations in which the radical pair singlet recombination rate, k_S, was varied, indeed show that, although the magnetic field at which the MFE is saturated for more than 90%, changes, the shape of the simulated MFE at lower field values seems to be conserved. If the MFE is simulated for different values of k_T, however, the shape of the MFE-curve changes drastically. Thus, we tentatively conclude that the observed changes are due to an increasing value of k_S as the temperature

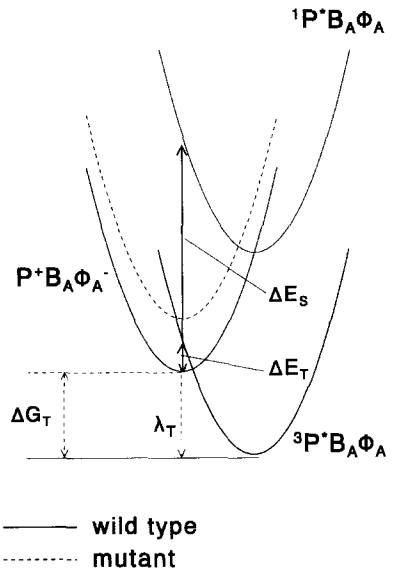

Fig. 9. Schematic drawing of the energy levels of the primary donor excited states and the charge-separated states of the RCs under study. The parabolas with the dashed line indicate the new energy levels of the mutant, which have been displaced by the mutation. The symbols are explained in the text.

increases [25,26]. The constant value of J indicates that the energies and interactions that influence the exchange interaction do not change with temperature.

The exchange interaction J is given by

$$2J = \delta E_S - \delta E_T \quad (9)$$

with δE_S and δE_T the energy shifts of the singlet and triplet states of $P^+B_A\Phi_A^-$, arising from their interactions with $^1P^*$ and ^3P, respectively [27] (Fig. 9). To first approximation, $^1[P^+B_A\Phi_A^-]$ is shifted to lower energies with respect to the unperturbed radical pair states by $\delta E_S = V_S^2/\Delta E_S$, with V_S the electronic coupling and ΔE_S the vertical energy difference between the $^1P^*B_A\Phi_A$ and the $P^+B_A\Phi_A^-$ level, evaluated at the equilibrium position of the latter state. Similarly, $^3[P^+B_A\Phi_A^-]$ shifts $\delta E_S = V_T^2/\Delta E_T$, with ΔE_T the vertical energy difference between the $^3P^*B_A\Phi_A$ and the $P^+B_A\Phi_A^-$ level. The sign of ΔE_T sensitively depends on the relative magnitude of the difference in free energy ΔG_T and the reorganization energy λ_T corresponding to charge recombination to ^3P.

In RCs of *Rb. sphaeroides*, ΔE_T is supposed to be very small (because the temperature dependence of k_T reflects an activationless transfer rate [10]) and positive, because only then will ΔE_T reduce the shift ΔE_S, and will the value of $2J$ calculated with second-order perturbation theory approach the measured values of the exchange interaction [27]. Apparently, the M210 Tyr → Trp mutation shifts the radical pair energy level closer to the $^1P^*$ level and further from the ^3P level, changing ΔE_T and reversing its sign (as ΔG_T can easily become larger than λ_T, Fig. 9).

In addition to an effect on the radical pair energy levels through altering the redox potential of P/P^+ [6], the mutation may also change the electron transfer matrix elements V_S and V_T. Some indication for this has come from an LD-ADMR study of the mutant, which showed that B_A is either slightly displaced or somewhat rotated with respect to P [3]. In view of the fact, however, that the mutant's charge separation rate is temperature activated [3,7], which is readily explained by an upward displacement of the $P^+B_A^-\Phi_A$ and $P^+B_A\Phi_A^-$ levels (Fig. 9), the latter effect probably predominates.

Recently, Volk et al. [28] proposed an extended second-order perturbation theory treatment, in which J was calculated in the Born-Oppenheimer approximation, including averaging over the vibrational states of the $P^+B_A\Phi_A^-$ state. For small values of ΔE_T as in *Rb. sphaeroides* wild type, this treatment avoids blowing up the second term in Eq. 9, and yields reasonable values of $2J$. In that case, the treatment predicts a strong temperature dependence of J. For larger values of ΔE_T, the temperature dependence of J is much smaller, and the method of Volk et al. and the simple perturbative approach discussed above are equivalent [28]. This appears to be the case for the M210 Tyr → Trp mutant, as $2J$ is only slightly temperature dependent (Fig. 6).

6. Conclusions

The linear-dichroic Magnetic Field Effect is shown to be a usefool tool to measure magnitude and sign of the radical pair singlet-triplet splitting $2J$.

The Tyr M210 → Trp mutation of *Rb. sphaeroides* wild type gives rise to a two-fold increase in $2J$, from 1.4 to 2.3-2.7 mT, and to a change of its sign, from positive in the native RCs to negative in mutant RCs. These effects are qualitatively explained by a mutation-induced increase of the energy of the charge-separated state.

The width of the B-curve of the MFE effect is little temperature dependent, indicating that the recombination rate to ^3P, k_T, is practically activationless. Because the concentration of ^3P depends quite strongly on the temperature, this dependence must be caused largely by activated recombination to the singlet ground state of P.

Acknowledgements

This work was supported by the Netherlands Foundation for Chemical Research (SON), financed by the Netherlands Organization for Scientific Research (NWO), and by Twinning Grant no. SCI*-CT90-0569 of the European Commission. SJS and PJH are grateful to Dr. D.A. Hunter and Dr. G. Zwanenburg, who both did a great deal of preliminary work on the MFE simulations.

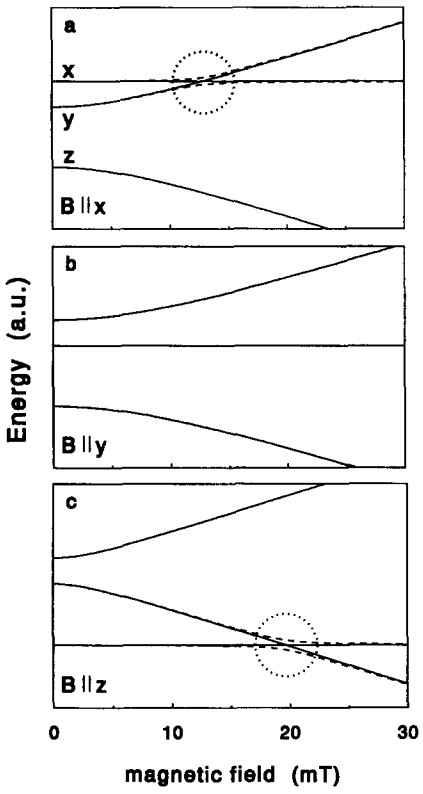

Fig. 10. Triplet energy levels as a function of the magnetic field, with the principal triplet axes oriented exactly parallel to the magnetic field B (drawn line) and almost pararallel (5°) to B (dashed line). (a) Triplet x-axis parallel to B. (b) Triplet y-axis parallel to B. (c) Triplet z-axis parallel to B.

Appendix 1

A calculation of the low-temperature magnetic field effect

The complicated calculations carried out for the simulations of Figs. 7 and 8, including diagonalising the Hamiltonian of ^{3}P and averaging over all orientations, do not provide much insight in the relation between the physical parameters and the observed (LD-)MFE. Therefore, we will present a simplified approach, by which the magnetic field dependence can be understood in a straightforward way. In this simplified model, we assume that the radical pair has no other decay channel but to ^{3}P, and calculate the MFE for the situations in which one of the triplet axes is nearly parallel to the magnetic field, at a few strategic magnetic field strengths.

The energy levels of ^{3}P as a function of the magnetic field are shown in Fig. 10 for the field directed along one of the principal axes of the zero-field splitting tensor (drawn lines; D = +20.0 mT, E = +3.5 mT). When the field is parallel to the z-axis, there is a crossing of state $|2>$ and $|3>$ (labelling the levels 1..3 from high to low energies) at approx. 20.0 mT. When the field is parallel to the x-axis, states $|1>$ and $|2>$ cross near 12.5 mT. If the field directions are changed 5°, the level crossings become *avoided* crossings (dashed lines, Fig. 10). The states that simply cross when the field is directed along the triplet z- or x-axis, mix when the field deviates from the principal axes. Thus, close to 12.5 mT (field almost parallel ($\sim \|$) to the x-axis) and 20.0 mT ($\sim \|$ z-axis) *the wavefunctions of ^{3}P are changing rapidly with the magnetic field.* These changes are observed for all orientations of the triplet relative to the magnetic field, except at precisely parallel orientations (solid lines, Fig. 10).

We will now calculate the MFE when one of the principal axes is oriented 'almost parallel' to the magnetic field, for zero magnetic field strength, infinite magnetic field strength, and B = 12.5 and 20.0 mT, the field values at which the (avoided) crossings occur for $B \sim \|$ the triplet x- and z-axis, respectively.

1. High field limit ($B \gg |J|, |D_{PI}|$)

In the high field limit, only ST_0 mixing will occur in the radical pair, as the $^3RP_{\pm 1}$ levels are far removed from the ^{1}RP-level by the Zeeman energy. We will calculate the triplet populating probability, p^∞, for a magnetic field sufficiently high that the high field limit applies.

When B is almost parallel to the triplet z-axis we can ignore the slight B-induced admixture of the other levels, $|T_0> = |T_z>$ and the only contribution to p^∞ is p_z^∞. Thus, with $k_3 = k_z$ and $[^3RP_3] = p_z^\infty$, the relative triplet population is given by:

$$[T] = k_T \sum_i \frac{[^3RP_i]}{k_i} = k_T p_z^\infty / k_z \qquad \text{(A1)}$$

and similarly for the magnetic field directed along one of the other two principal axes:

$$[T] = k_T p_i^\infty / k_i, i = x, y, z \qquad \text{(A2)}$$

Assuming that the radical pair is isotropic (i.e. $D_{PI} = 0$), we have

$$p_x^\infty = p_y^\infty = p_z^\infty \qquad \text{(A3)}$$

and the relative triplet concentration for a high magnetic field directed along one of the principal axes is given by:

$$[T] = k_T p_z^\infty / k_i, i = x, y, z. \qquad \text{(A4)}$$

2. Triplet concentration in zero magnetic field

In zero field, and for $|J| \gg |D_{PI}|$, the three ^{3}RP-levels will all be at approx. the same energy distance from the ^{1}RP level, and singlet-triplet mixing will be similar for all three levels. The zero-field states then will be populated equally:

$$p_x = p_y = p_z. \qquad \text{(A5)}$$

Because k_T is much larger than the rate of singlet-triplet mixing, and k_S is very slow at low temperatures, the ^{3}RP states decay exclusively by recombination to ^{3}P, for all magnetic fields. It follows that

$$p_x + p_y + p_z = p_z^\infty, \qquad \text{(A6)}$$

and

$$p_x = p_y = p_z = \tfrac{1}{3}p_z^{\infty} \quad \text{(A7)}$$

The decay rates related to each ^{3}P sublevel are by definition k_x, k_y and k_z, so that the relative triplet concentration becomes

$$[T] = k_T \tfrac{1}{3} p_z^{\infty} \left(\frac{1}{k_x} + \frac{1}{k_y} + \frac{1}{k_z} \right). \quad \text{(A8)}$$

3. Field almost parallel to z-axis, B = 20.0 mT

This is the magnetic field strength at which the avoided crossing between states $|2>$ and $|3>$, shown in Fig. 10c, takes place. For simplicity, we assume that the high-field approximation still applies. In the high-field limit, the triplet populating probability and decay rates are given by [29]:

$$k_1 = k_2 = \tfrac{1}{2}(k_x + k_y), k_3 = k_z \quad \text{(A9a)}$$

$$[^3\mathrm{RP}_1] = [^3\mathrm{RP}_2] = 0, [^3\mathrm{RP}_3] = p_z^{\infty} \quad \text{(A9b)}$$

Since state $|1>$ is not involved in the crossing, its wavefunction does not change around 20.0 mT and in the high-field limit it is not populated. States $|2>$ and $|3>$, however, mix completely at 20.0 mT, resulting in averaging both the decay rates k_2 and k_3, and the populating probabilities p_2 and p_3, of ^{3}P. Thus, at the avoided crossing at 20.0 mT the triplet decay rates and ^{3}RP sublevel populations are

$$k_1 = \tfrac{1}{2}(k_x + k_y); [^3\mathrm{RP}_1] = 0 \quad \text{(A10a)}$$

$$k_2 = k_3 = \tfrac{1}{4}(k_x + k_y) + \tfrac{1}{2}k_z; [^3\mathrm{RP}_2] = [^3\mathrm{RP}_3] = \tfrac{1}{2}p_z^{\infty} \quad \text{(A10b)}$$

which yields

$$[T] = \frac{4k_T p_z^{\infty}}{k_x + k_y + 2k_z}. \quad \text{(A11)}$$

4. Field almost parallel to the x-axis, B = 12.5 mT

Using again the high-field approximation, we cyclicly permute $z \rightarrow x \rightarrow y \rightarrow z$ and obtain

$$[T] = \frac{4k_T p_z^{\infty}}{k_y + k_z + 2k_x}. \quad \text{(A12)}$$

Table 1
Triplet concentrations, expressed in units of $k_T p_z^{\infty}/k_z$, for the triplet x-, y- and z-axis oriented almost parallel to the magnetic field for the four 'strategic' magnetic field strengths discussed in the Appendix

	$B \sim \parallel x$	$B \sim \parallel y$	$B \sim \parallel z$
$B = 0$	0.44	see $B \sim \parallel x$	see $B \sim \parallel x$
$B = 12.5$ mT	0.21	see $B = \infty$	see $B = \infty$
$B = 20.0$ mT	see $B = \infty$	see $B = \infty$	0.29
$B = \infty$	0.17	0.17	1.0

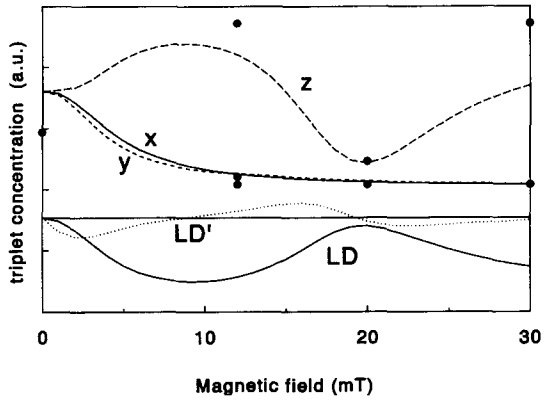

Fig. 11. Relative triplet concentrations for the cases when the triplet principal axes are almost parallel to the magnetic field for the triplet x-axis (drawn line) y-axis (short-dashed line) and z-axis (long-dashed line) calculated with the exact model. The LD−MFE-curve (LD) and its derivative (LD') were calculated using the triplet concentrations shown, and the expression for the LD-MFE given in the Appendix (Eq. A13). Indicated are the values obtained with the crude approximations described in the Appendix (●).

The results of the above approximate calculations are summarised in Table 1. Using the experimental evidence that $k_x \approx k_y \approx 6\ k_z$ [16,30], we express the triplet concentration for each orientation in units of $k_T p_z^{\infty}/k_z$. The graphical representation is shown in Fig. 11. It is seen that there is a large effect at 20.0 mT, when B is almost parallel to the triplet z-axis, and that there is a much smaller feature at 12.5 mT, when B is almost parallel to the x-axis.

The experimental LD-signal is related to $[T]$ by an integral in which the weighting factors are determined by the excitation and absorption properties of the molecules, which are dependent on the orientation of the optical transition moment relative to the light vector (see above). Experimentally, $\vec{\nu}$ is parallel or perpendicular to the magnetic field. From LD-ADMR experiments [3,31], it is known that the optical Q_y transition moment is approximately parallel to the triplet y-axis. We therefore approximate the MFE recorded for ν parallel to the magnetic field by the MFE for B directed (almost) along the triplet y-axis, and for ν perpendicular to B by half the sum of the MFE for $B_0 \sim \parallel x$ and $B_0 \sim \parallel z$. The LD-MFE is then approximated by

$$LD = [T]_{B \sim \parallel y} - \tfrac{1}{2}([T]_{B \sim \parallel x} + [T]_{B \sim \parallel z}), \quad \text{(A13)}$$

which results in the LD-MFE-curve shown in Fig. 11. It is seen that the LD-signal is dominated by the effect of the avoided crossing at ~ 20.0 mT, when B is almost parallel to the triplet z-axis.

References

[1] Hoff, A.J., Lous, E.J., Moehl, K.W. and Dijkman, J.A. (1985) Chem. Phys. Lett. 114, 39–43.

[2] Williams, J.C., Steiner, K.A. and Feher, G. (1986) in Proteins: Structure, Function and Genetics 1, 312–325.
[3] Shochat, S., Arlt, Th., Francke, Chr.,Gast,, P., Van Noort, P.I., Otte, S.C.M., Schelvis, J.P.M., Schmidt, S., Vijgenboom, E., Vrieze, J., Zinth, W. and Hoff, A.J. (1994) Photosynth. Res. 40, 155–166.
[4] Gray, K.A., Farchaus, J.W., Wachtveitl, J., Breton, J. and Oesterhelt, D. (1990) EMBO J. 9, 2061–2070.
[5] Finkele, U., Lauterwasser, C., Zinth, W., Gray, K.A. and Oesterhelt, D. (1990) Biochemistry 29, 8517–8521.
[6] Nagarajan, V., Parson, W.W., Gaul, D. and Schenck, C. (1990) Proc. Nat. Acad. Sci. USA 87, 7888–7892.
[7] Van Noort, P.I., Shochat, S., Schmidt, S., Arlt, T., Schelvis, H.P.M., Gast, P., Aartsma, T.J., Amesz, J. and Hoff, A.J. (1995) Photosynth. Res., in the press.
[8] Hoff, A.J., Gast, P., Van der Vos, R., Vrieze, J., Franken, E.M. and Lous, E.J. (1992) in Magnetic Field and Spin Effects in Chemistry and Related Phenomena, Germany.
[9] Shochat, S., Van Noort, P.I., Van der Vos, R., Otte, S.C.M., Schelvis, J.P.M., Vrieze, J., Gast, P. and Hoff, A.J. (1992) in (Murata, N., ed.), pp. 413–416, Kluwer, Dordrecht.
[10] Ogrodnik, A., Remy-Richter, N., Michel-Beyerle, M.E. and Feick, R. (1987) Chem. Phys. Lett. 135, 576-581.
[11] Lersch, W. and Michel-Beyerle, M.E. (1989) in Advanced EPR. Applications in Biology and Biochemistry (Hoff, A.J., ed.), pp. 685–705, Elsevier, Amsterdam.
[12] Martin, J.L., Breton, J., Hoff, A.J., Migus, A. and Antonetti, A. (1986) Proc. Natl. Acad. Sci. USA 72, 2251–2255.
[13] Werner, H.-J., Schulten, K. and Weller, A. (1978) Biophys. Biochim. Acta 502, 255–268.
[14] Haberkorn, R. and Michel-Beyerle, M.-E. (1979) Biophys. J. 26, 489–498.
[15] Hoff, A.J. (1981) Q. Rev. Biophys. 14, 599–665.
[16] Hoff, A.J. (1976) Biochim. Biophys. Acta 440, 765–771.
[17] Lous, E.J. and Hoff, A.J. (1988) in The Photosynthetic Bacterial Reaction Center - Structure and Dynamics (Breton, J. and Verméglio, A., eds.), Plenum, New York.
[18] Lous, E.J. and Hoff, A.J. (1986) Photosynth. Res. 9, pp. 89–101.
[19] Van Kan, P.J.M. (1991) Doctoral Thesis, Leiden University.
[20] Rao, M.G. (1982) in: Temperature, its Measurement and Control in Science and Industry, Vol. 5, pp. 1205–1211, American Institute of Physics, New York.
[21] Schenck, C.C., Blankenship, R.E. and Parson, W.W. (1982) Biochim. Biophys. Acta 680, 44–59.
[22] Lous, E.J. and Hoff, A.J. (1989) 88–103.
[23] Hore, P.J., Riley, D.J., Semlyen, J.J., Zwanenburg, G. and Hoff, A.J. (1993) Biochim. Biophys. Acta 1141, 221–230.
[24] Cogdell, R.J., Monger, T.G. and Parson, W.W. (1975) Biochim. Biophys. Acta 408, 189–199.
[25] Budil, D.E., Kolaczkowski, S.V. and Norris, J.R. (1987) in: Progress in Photosynthesis Research (Biggins, J., ed.), Vol. I, pp. 25–27, Martinus Nijhoff, Dordrecht.
[26] Ogrodnik, A., Volk, M., Letterer, R., Feick, R. and Michel-Beyerle, M.E. (1988) Biochim. Biophys. Acta 936, 361–371.
[27] Bixon, M., Jortner, J. Michel-Beyerle, M.E. and Ogrodnik, A. (1989) 273–286.
[28] Volk, M., Häberle, T., Feick, R., Ogrodnik, A. and Michel-Beyerle, M.E. (1993) J. Phys. Chem. 97, 9831–9836.
[29] Wertz, J.E., Bolton, J.R. (1972) Electron Spin Resonance, Elementary Theory and Practical Applications, McGraw-Hill, New York.
[30] den Blanken, H.J., Jongenelis, A.D.J.M. and Hoff, A.J. (1983) Biochim. Biophys. Acta 725, 472–482.
[31] Lous, E.J. and Hoff, A.J. (1987) Proc. Natl. Acad. Sci. USA 84, 6147–6151.